Acta Metall. Sin. (Engl. Lett.), 2015, **28**(2), 139–146
DOI 10.1007/s40195-014-0174-8

Influence of Rust Layers on the Corrosion Behavior of Ultra-High Strength Steel 300M Subjected to Wet–Dry cyclic Environment with Chloride and Low Humidity

Qiang Guo · Jian-Hua Liu · Mei Yu · Song-Mei Li

Received: 4 March 2014 / Revised: 17 May 2014 / Published online: 18 November 2014

Abstract The influence of rust layers on the corrosion behavior of ultra-high strength steel 300M subjected to a simulated coastal atmosphere was investigated by corrosion weight loss, surface analysis techniques, and electrochemical methods. The results exhibit the presence of a large proportion of γ-FeOOH and α-FeOOH and a small amount of Fe_3O_4 in the outer rust layer. During the wet–dry cyclic process, the bonding performance and the density of outer rust layer deteriorate with the thickness of outer rust. The inner rust layer plays a main role on protectiveness, which can be attributed to the formation of an ultra-dense and adherent rust film with major constituent of α-FeOOH and α-Fe_2O_3 on the steel.

KEY WORDS: Ultra-high strength steel; Wet–dry; Chloride; Corrosion; Rust

1 Introduction

It has been widely accepted that typical atmospheric corrosion acts as an alternate wet–dry corrosion process [1, 2]. Some mechanism models for atmospheric corrosion have been developed [2–6]. Costal and marine atmospheric environments with abundant air-borne chloride are very important service sites for structural steels. Corrosion behavior of steels in chloride-rich atmospheric environments has attracted wide attention.

In the past decades, most work for atmospheric corrosion focused on outdoor exposure corrosion [7–12]. Long-term outdoor exposure tests could provide reliable and abundant information for atmospheric corrosion. However, the results obtained have a large scatter in different locations. Moreover, it normally takes several years or even several decades. Laboratory-accelerated corrosion test is an appropriate method for rapid, comprehensive, and exact evaluation, which could be operated with identical environmental factors in different locations [13–16].

Zhao et al. [15] reported that the microstructure of steels affected corrosion resistance in wet–dry cyclic corrosion environment. Hao et al. [16] noticed that the composition and electrochemical properties of rust affected corrosion rate of weathering steels in simulated coastal environment. Nishimura et al. [17] pointed out that in cyclic wet–dry corrosion environment with chloride, nano-scale iron oxide in inner rust layer on weathering steel increased corrosion resistance. Sun et al. [18] investigated corrosion behavior of ultra-high strength steel 300M by salt spraying corrosion test and found that the porous outer rust with main composition γ-FeOOH could accelerate corrosion rate. However, research on rusting mechanism of low alloy martensitic steel in wet–dry cyclic environments has rarely been reported.

300M is recognized as a most successful low alloy ultra-high strength steel in the application of aircraft landing gears. In the past decades, it has been widely applied in aerospace and also other industries. During long-term service of the steel in costal and marine atmosphere, it is imperative to explore the alternate wet–dry corrosion

Available online at http://link.springer.com/journal/40195

Q. Guo · J.-H. Liu (✉) · M. Yu · S.-M. Li
Key Laboratory of Aerospace Materials and Performance (Ministry of Education), School of Materials Science and Engineering, Beihang University, Beijing 100191, China
e-mail: liujh@buaa.edu.cn

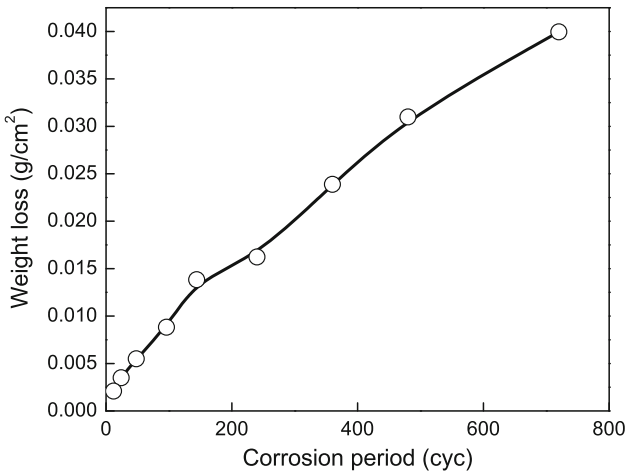

Fig. 1 Corrosion weight loss of 300M with different CCT cycles in the wet–dry cyclic environment

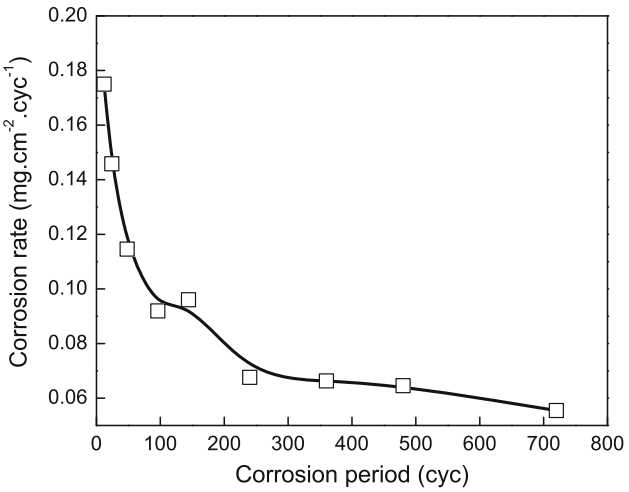

Fig. 2 Corrosion rate of 300M with different CCT cycles in the wet–dry cyclic environment

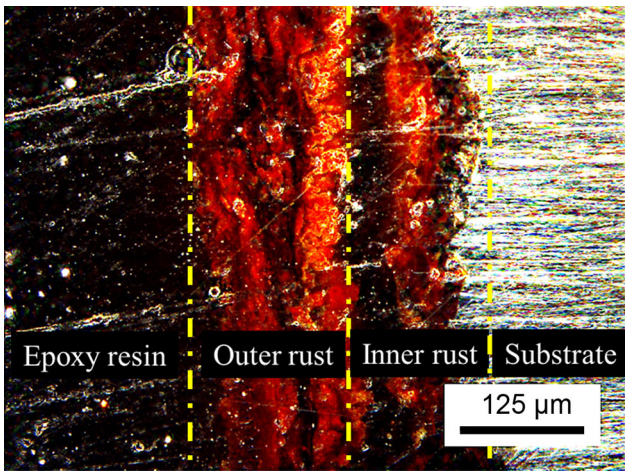

Fig. 3 OM cross-sectional morphology of rust layers on 300M exposed for 144 cyc CCT

behavior of the steel from the consideration of minimum maintenance and service safety.

In the present work, an alternate wet–dry accelerated corrosion test was employed to investigate the corrosion behavior of an ultra-high strength steel 300M in the costal atmosphere with moderate aggressivity at 27 °C and 45% RH (relative humidity). In particular, the work focused on the formation and the protectiveness of rust layers on the steel in the environment.

2 Experimental

2.1 Materials

The main chemical composition of ultra-high strength steel 300M is shown as follows (wt%): 0.40 C, 1.90 Ni, 0.71 Cr, 1.66 Si, 0.64 Mn, 0.37 Mo, 0.088 V, and balance of Fe. The microstructure of the steel mainly contained lath/plate martensite with M_7C_3, ε-carbides in the substrate and along boundaries, and retained austenite at prior austenite grain boundaries [19–22]. In order to ensure the reliability of experimental data, three samples (60 mm × 30 mm × 3 mm) were used for the measurement of corrosion weight loss, leaving an exposure area of 50 mm × 25 mm with other area sealed by styrene-butadiene rubber. The exposure surface was mechanically ground with SiC emery paper up to grade 1000#. All the samples were cleaned in acetone by ultrasonic sound, dried by cold air flow, and stored in a desiccator.

2.2 Wet–Dry Cyclic Corrosion Test (CCT)

Referred to ASTM G 44-99 [23], one CCT cycle involves two stages: (1) the samples were immersed in 3.5 wt% NaCl solution at (27 ± 1) °C for 10 min and (2) the samples were subsequently dried for 50 min at (45 ± 2)% RH and (27 ± 1) °C. The experimental solution was refreshed for 48 h.

The rust on the steel was completely removed by dipping in a mixed solution with 500 mL HCl, 500 mL H_2O, and 3.5 g $C_6H_{12}N_4$. After that, the samples were weighed before CCT and after rust removal to determine the corrosion weight loss.

2.3 Electrochemical Measurements

The electrochemical measurements were performed on an electrochemical working station (VersaSTAT MC-4, Ametek , USA) in neutral 3.5 wt% NaCl solution at room temperature [25 ± 2 °C], using a traditional three-electrode electrolytic cell with a Pt plate as counter electrode, a

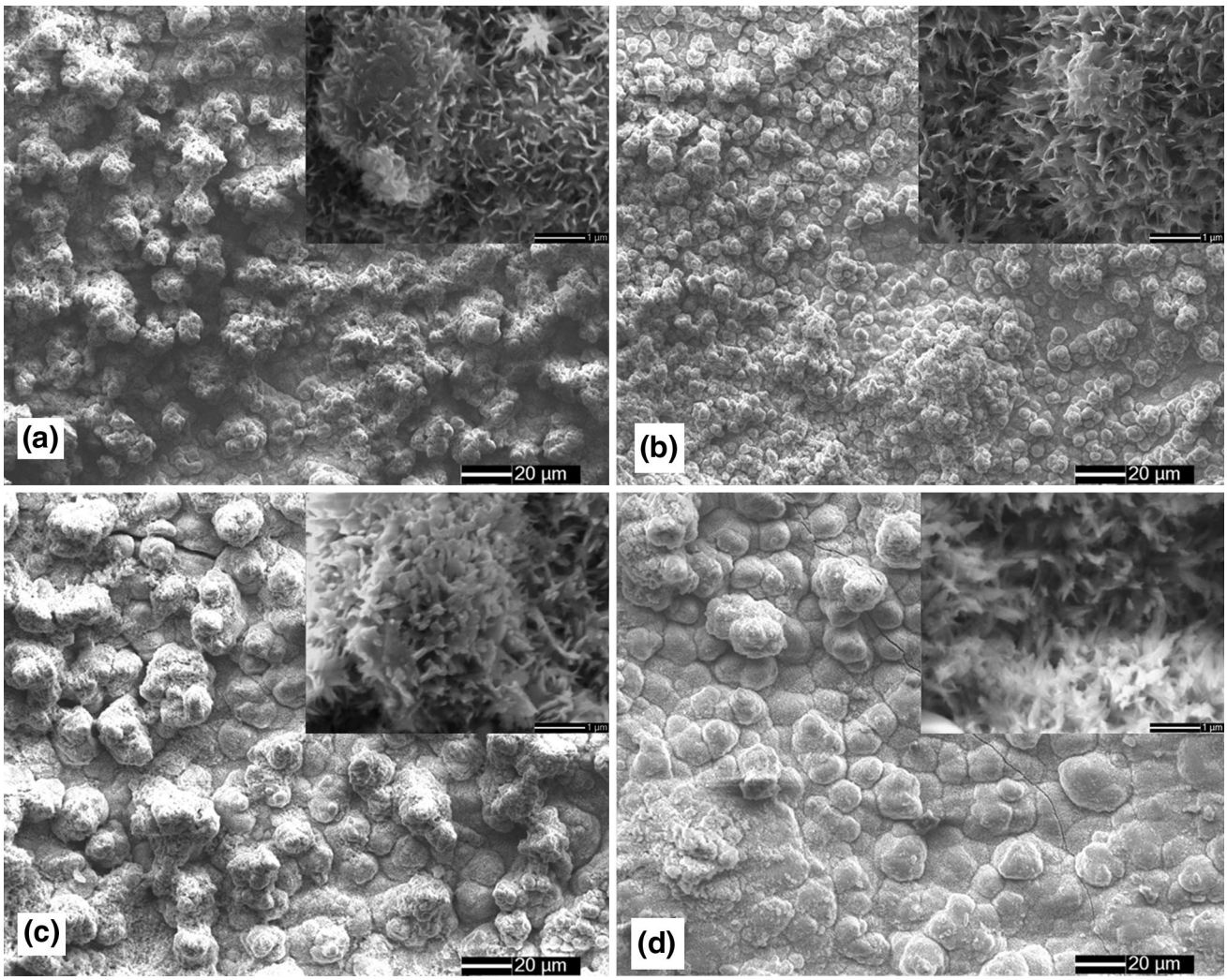

Fig. 4 The surface morphology of outer rust after different CCT cycles: **a** 144 cyc; **b** 240 cyc; **c** 480 cyc; **d** 720 cyc

KCl saturated calomel electrode (SCE) as reference electrode and the rusted steel as a working eletrode. Open circuit potential (E_{oc}) was measured for at least 1 h before potential stabilization. Electrochemical impedance spectroscopy (EIS) was applied in 10 mV sinusoidal voltage and a frequency range from 100 kHz to 10 mHz. The potentiodynamic polarization measurement was performed from −250 mV (vs. E_{oc}) to 200 mV (vs. E_{ref}) at a sweep rate of 0.5 mV/s.

2.4 Structural and Compositional Characterization

Surface morphology of outer and inner rust layers was observed by field emission scanning electron microscope (FE-SEM, Apollo300, SanCam, UK). The section morphology of the rusted steel was observed by an optical microscope (OM, LeiCa DM4000M, Germany) with a dark field mode. The outer rust was ground into fine powders and detected by X-ray Diffraction (XRD, D/max-2200, Rigaku, Japan) using Cu as the target with an electric current of 200 mA and a voltage of 40 kV at a scanning rate of 3°/min. Laser Raman spectroscopy (Lab RAM HR800, Horiba JR, France) was used to characterize the composition of the inner and outer rust layers on the steel, which was operated with argon ion laser as an excitation source ($\lambda = 614$ nm).

3 Results

3.1 Corrosion Kinetics

Figure 1 shows a curve of corrosion weight loss results with respect to CCT cycles. The curve follows the well-known bi-logarithmic formula, as shown in Eq. (1). The corrosion rate (vs. CCT cycles) is calculated according to Eq. (2), as shown in Fig. 2.

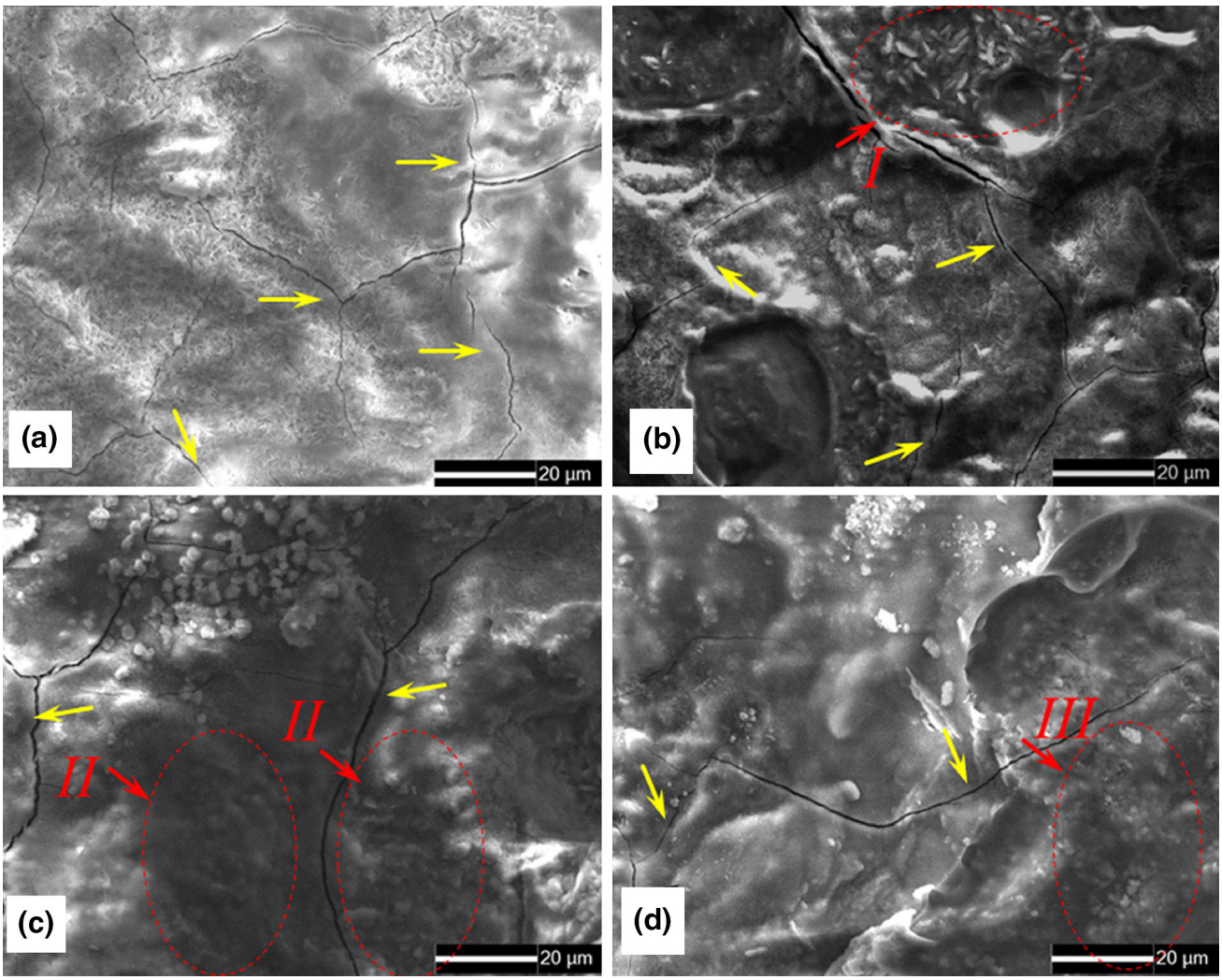

Fig. 5 The surface morphology of inner rust after different CCT cycles: **a** 144 cyc; **b** 240 cyc; **c** 480 cyc; **d** 720 cyc

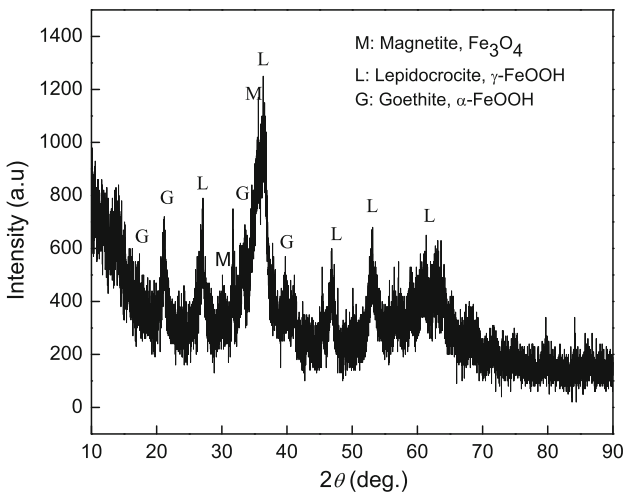

Fig. 6 XRD pattern of outer rust on steel 300M exposed for 480 CCT cycles

$$\Delta w = \frac{W_b - W_a}{S} = A \times t^n = 3.22282\text{E} - 4 \times t^{0.73364}. \quad (1)$$

$$v = \frac{\Delta w}{t} \times 1000, \quad (2)$$

where Δw is the corrosion weight loss, v denotes corrosion rate of the steel (vs. CCT cycles), W_b is the corrosion weight before corrosion test, W_a is the corrosion weight after rust removal, S is the exposure area on the sample, A and n denotes constants and t denotes the number of CCT cycles. The value n means the protective effectiveness; when $0 < n < 1$, it means that the rust on the steel is protective against corrosion.

In Fig. 2, corrosion rate decreases when CCT cycle increases from 0 to 720 cyc. A high corrosion rate is observed within 0–144 cyc. An apparent decline of corrosion rate is noted within the range of 144 to 240 cyc. The

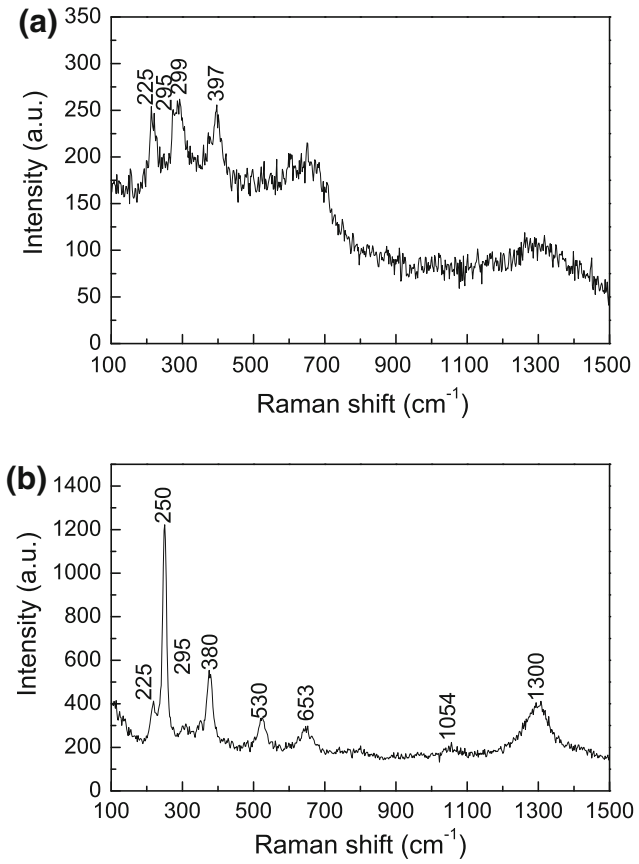

Fig. 7 Raman spectra of inner **a** and outer **b** rust layers on 300M exposed for 480 CCT cycles

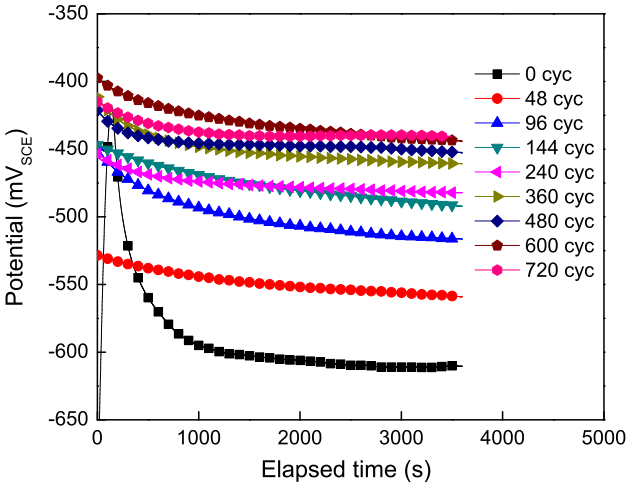

Fig. 8 Open circuit potential of rusted steel 300M exposed for different CCT cycles

corrosion rate was kept at low value with 240 to 720 cyc. Based on the value $n = 0.73$ in formula (1), it is predicted that the rust has inhibition effect against corrosion.

3.2 Rust Morphologies

Figure 3 shows optical microscopic cross-sectional morphology of rust layer for 144 CCT cycles. The rust layer could be identified as outer and inner rust layers. The outer rust layer is compact but shows a layer-by-layer structure. The inner rust layer is very dense.

All the images of outer rust in Fig. 4 were taken from the similar location of rusted steels after 144, 240, 480, and 720 CCT cycles, respectively. Surficial rust after 144 cyc begins to agglomerate into particles without regular size. The amplificatory image in Fig. 4a shows acicular sphere particles. Corrosion product grows into small regular spheres after 240 cyc (Fig. 4b). According to an enlarged image of Fig. 4b), the small acicular sphere connects with each other. Up to 480 cyc, the spherical particles grow larger and congregate into a compact rust layer. The amplificatory image of Fig. 4c shows that acicular morphology of the spheres becomes brushy. After 720 cyc, spherical particles are integrated into a more compact and even film, as shown in Fig. 4d. The enlarged image of Fig. 4d shows denser acicular morphology on the spherical particles. The magnified images in Fig. 4a–d show the same acicular morphology, which means that the surficial rust is composed of the identical constituent.

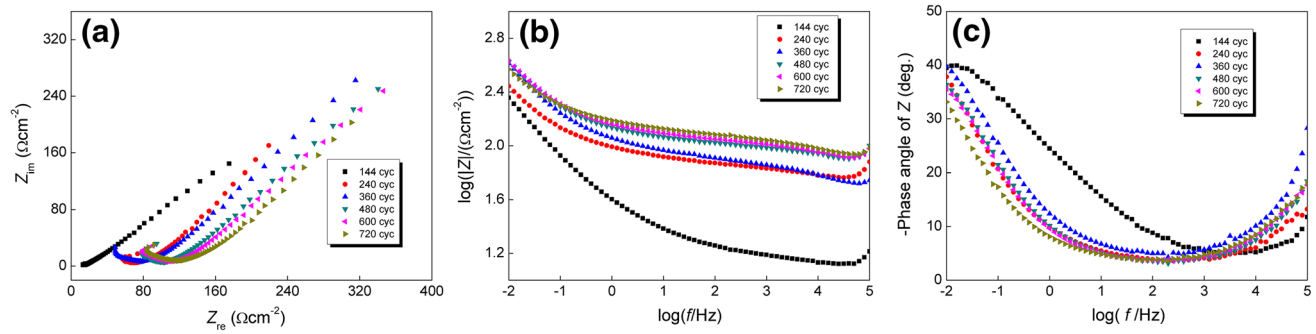

Fig. 9 EIS diagrams of rusted steel 300M exposed for different CCT cycles: **a** Nyquist plots; **b** Bode plots of log|*Z*| versus log*f*; **c** Bode plots of -Phase angle versus log*f*

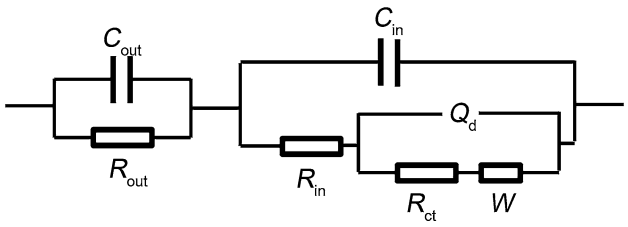

Fig. 10 Equivalent circuit diagram for EIS diagrams of rusted steel 300M exposed for different CCT cycles

Figure 5(a-d) show the surface morphology of inner rust on the steel formed after 144, 240, 480, and 720 cyc of CCT, respectively. The surface of the inner rust after 144 cyc shows brushy appearance, many cracks are observed (Fig. 5a). Quite fewer cracks are observed on the surface of inner rust after 240 cyc. Region I in Fig. 5b shows that flake corrosion product has been formed in the inner rust. Up to 480 cyc, the surface of inner rust appears smooth and denser. The surface of inner rust after 720 cyc is much denser, with much fewer cracks. Regions II and III in Fig. 5c and d show that the dense inner rust contains particle corrosion product. With the increase of CCT cycles, the inner rust surface becomes smooth. The boundary between the inner and the outer rust becomes more and more apparent.

3.3 Rust Composition

The outer rust exposed for 480 cyc of CCT was analyzed by XRD, as shown in Fig. 6. It is observed that the outer rust is mainly composed of γ-FeOOH, α-FeOOH, and Fe_3O_4. The intensity of γ-FeOOH is stronger than that of α-FeOOH, implying a larger content of γ-FeOOH than α-FeOOH in the outer rust.

Raman spectra of the inner and outer rust on the samples after 480 cyc of CCT are shown in Fig. 7. The peaks at 299 and 397 cm^{-1} are identified as α-FeOOH [24–26]; the peaks at 225 and 295 cm^{-1} are confirmed as α-Fe_2O_3 [24–28]. Peaks at 252, 380, 528, 654, 1,054, and 1,307 cm^{-1} are characteristic ones of γ-FeOOH [24–28]. It indicates that γ-FeOOH and α-Fe_2O_3 distribute in the surficial layer of the outer rust and α-FeOOH is the main composition of the inner rust, with a small proportion of α-Fe_2O_3 and Fe_3O_4.

In all, the inner rust is composed mainly of α-FeOOH, with some α-Fe_2O_3 and Fe_3O_4. The outer rust consists of a large amount of γ-FeOOH and a small amount of α-FeOOH and Fe_3O_4. The surficial rust is believed to be γ-FeOOH.

3.4 Electrochemical Measurements

Figure 8 shows OCP curves of the rusted steel exposed for different CCT cycles. The naked steel before CCT shows low OCP value at -600 mV_{SCE}. With CCT proceeding, OCP gradually shifts to noble values and remains unchanged at -440 mV_{SCE} after 360 cyc.

Figure 9 shows Nyquist and Bode plots of EIS diagrams of the rusted steel during 144–720 cyc. The equivalent circuit corresponding to the EIS diagrams is shown in Fig. 10, where symbols R_{out} and R_{in} denote the impedance of the outer and the inner rust, respectively; C_{out} and C_{in} denote the capacitance of the outer and the inner rust, respectively; R_{ct} is charge transfer resistance; W is diffusion impedance; Q_d is double-layer capacitance, and constant phase element (CPE) substitutes Q_d during the actual simulation, which includes Y and n; Y is model value of Q_d; and n is dispersion coefficient, $0 < n < 1$. The values R_{out}, R_{in}, R_{ct}, and W are suggested to be the most useful indicators to estimate the protectiveness of the rust layer [29]. The simulated results for all parameters are listed in Table 1.

The curves of four symbols R_{out}, R_{in}, R_{ct}, and W as a function of CCT cycles are shown in Fig. 11, respectively. R_{out}, R_{in}, R_{ct}, and W increase from 144 to 720 CCT cycles, with the exception of R_{out} for 480 CCT cycles in Fig. 11a. It indicates that with CCT proceeding, corrosion resistance of the outer and the inner rust layer increases remarkably. The abnormal value of R_{out} for 480 CCT cycles is related to the peeling off of the outer rust layer.

Figure 12 shows potentiodynamic polarization curves exposed for different CCT cycles. When rust covered the whole surface of the sample, the reduction of corrosion

Table 1 Simulated results of EIS diagrams for different corrosion times

CCT cycle	C_{out} (10^{-8}F/cm^2)	R_{out} (Ω/cm^2)	C_{in} (10^{-6}F/cm^2)	R_{in}(Ω/cm^2)	Q (F/cm^2)	n	R_{ct}(Ω/cm^2)	W(Ω/cm^2)
144	4.26242	54.10191	15.121	5.75541	0.00511	0.76089	15.83439	0.01855
240	1.13682	61.47771	9.52994	7.56178	0.00345	0.76994	17.41401	0.01857
360	1.25452	81.74522	2.44586	13.1465	0.0016	0.75643	20.33121	0.01832
480	2.71592	53.73248	1.93631	14.44586	0.0013	0.74344	22.63694	0.01806
600	1.0679	84.36943	1.96051	15.7707	0.00141	0.74917	23.09554	0.01833
720	1.04611	88.12739	1.61274	18.15287	0.00205	0.66255	33.69427	0.02242

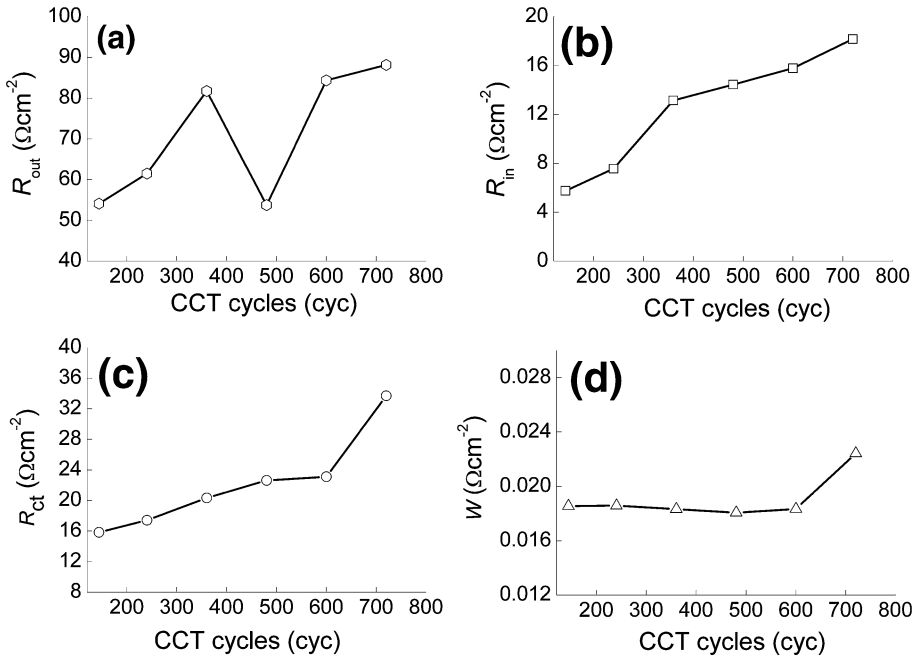

Fig. 11 The variation of R_{out} (a), R_{in} (**b**), R_{ct} (**c**), and W (**d**) obtained from EIS diagrams of steel 300M with different CCT cycles

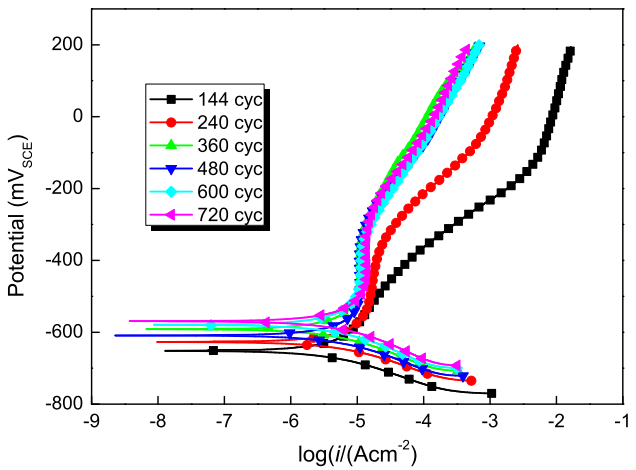

Fig. 12 Potentiodynamic polarization curves of rusted steel 300M exposed for different CCT cycles

product became dominant in the cathodic process. The slope of cathodic polarization branch nearly unchanged in 144–720 cyc. It indicates that the amount of γ-FeOOH stabilizes in 144–720 cyc. The corrosion potential E_{corr} increases when the corrosion time increases from 144 to 720 cyc. The slope of anodic polarization curve increases with corrosion time in 144–240 cyc and then remains almost unchanged in 360–720 cyc. The anodic current density decreases when CCT cycles increase from 144 to 720 cyc. As the rust thickness reached a certain value, anodic current in anodic region of potentiodynamic polarization curves was kept at a certain value in a certain potential range. It indicates that as rust overlays the steel surface, it mostly affected the anodic polarization process with CCT increasing.

4 Discussion

In the wet–dry cyclic environment, the outer rust layer was composed of main constituents of γ-FeOOH and α-FeOOH and a small amount of Fe_3O_4, which were commonly found to be the main composition of outer rust in outdoor costal atmosphere [7, 8]. The outer rust layer exhibited porous and poor adherence with inner rust after certain CCT cycles. That is to say that the density and bonding of outer rust layer were affected by the thickness of rust and drying process. Before 240 cyc, thin rust layer on the steel was dried totally. The rust layer showed excellent bonding and high density. Thick rust prolonged the evaporation time of the water in outer rust layer. After 480 cyc, the drying stage was insufficient for the drying up of the outer rust layer; rust beneath the surface was still wetted. Inhomogeneous wetness in the outer rust introduced defects beneath the surface, such as cavities and holes, which deteriorated the bonding and the density of the outer rust. Newly formed yellow-orange rust (γ-FeOOH) covered the surface of the outer rust with a quantity of defects. As a result, the rust in the top of the outer rust layer showed a layer-by-layer structure. Subsequently, the surficial rust heaved and even

broke off. Moreover, the yellow-orange rust would generate or flow in the defects, and then the defects could be self-repaired [30].

The inner rust layer showed an integrated dense film with main constituents of α-FeOOH and α-Fe_2O_3, which showed excellent bonding force with the steel. On the surface of inner rust, corrosion product in nano particles from the outer rust layer was accumulated and integrated into ultra-high dense rust film. The dense inner rust layer acted as a physical barrier for water, oxygen, chloride, etc.

Before 360 CCT cycles, the resistance R_{out} increased with the thickness of the outer rust layer. After 480 CCT cycles, R_{out} decreased due to the deterioration of the outer rust layer. By contrast, R_{in} increased with the increase of CCT cycles. The potentiodynamic polarization curves confirmed that the rust on the steel restrained the dissolution of iron. Corrosion rate obtained from the weight loss results decreased with CCT cycles very remarkably and remained stable at a small value. The electrochemical measurements were found to be consistent with corrosion weight loss results, which confirmed that the rust apparently decreased the corrosion rate of the steel.

Therefore, in the initial CCT period, the outer rust layer played main protectiveness on the steel; after the outer rust layer became porous and loose, the protectiveness degraded. Meanwhile, the dense inner rust layer adherent to the steel inhibited corrosion. In addition, the inner rust layer played an important role on corrosion resistance of the rusted steel during the whole CCT process.

5 Conclusions

In the wet–dry cyclic environment with chloride and low humidity, the corrosion behavior of ultra-high strength steel 300M is summarized as follows:

(1) The outer rust consists of a large amount of γ-FeOOH and α-FeOOH and a small amount of Fe_3O_4. With the increase of thickness of the outer rust, the outer rust shows porous and poor bonding force with the inner rust, which is mainly attributed to the insufficient drying of the thick rust during the CCT process.

(2) The inner rust layer is an ultra-dense film adherent to the steel with main composition of α-FeOOH and α-Fe_2O_3. The inner rust is transformed from nanostructure corrosion product in the outer rust.

3) During initial CCT period, the outer rust layer plays main protectiveness on the steel. The inner rust shows excellent corrosion inhibition and plays an important role on corrosion resistance during the whole CCT period.

Acknowledgments This work was financially supported by the National Natural Science Foundation of China (No. 51171011).

References

[1] M. Stratmann, Corros. Sci. **27**(86), 9 (1987)
[2] M. Stratmann, H. Streckel, Corros. Sci. **30**, 681 (1990)
[3] U.R. Evans, Nature **206**, 980 (1965)
[4] U.R. Evans, C.A.J. Taylor, Corros. Sci. **12**, 227 (1972)
[5] T. Misawa, K. Hashimoto, S. Shimodaira, Corros. Sci. **14**, 131 (1974)
[6] J. Dunnwald, A. Otto, Corros. Sci. **29**, 1167 (1989)
[7] Y.T. Ma, Y. Li, F.H. Wang, Corros. Sci. **51**, 997 (2009)
[8] Y.T. Ma, Y. Li, F.H. Wang, Corros. Sci. **51**, 1725 (2009)
[9] J. Guo, S.W. Yang, C.J. Shang, Y. Wang, X.L. He, Corros. Sci. **51**, 242 (2008)
[10] Q.X. Li, Z.Y. Wang, W. Han, E.H. Han, Acta Phys. Chim. Sin. **24**, 1459 (2008). (in Chinese)
[11] S. Syed, Mater. Corros. **61**, 238 (2010)
[12] S.T. Wang, S.W. Yang, K.W. Gao, X.L. He, Acta Metall. Sin. (Engl. Lett.) **21**, 425 (2008)
[13] F.L. Sun, X.G. Li, F. Zhang, X.Q. Cheng, C. Zhou, Acta Metall. Sin. (Engl. Lett.) **26**, 257 (2013)
[14] L.N. Xu, Y. Cheng, Y.G. Shi, Y. Liu, Acta Metall. Sin. (Engl. Lett.) **26**, 271 (2013)
[15] Y.T. Zhao, S.W. Yang, C.J. Shang, X.M. Wang, W. Liu, X.L. He, Mater. Sci. Eng. A **454–455**, 695 (2007)
[16] L. Hao, S.X. Zhang, J.H. Dong, W. Ke, Corros. Sci. **58**, 175 (2012)
[17] T. Nishimura, H. Katayama, K. Noda, T. Kodama, Corros. Sci. **42**, 1611 (2000)
[18] M. Sun, K. Xiao, C.F. Dong, X.G. Li, Acta Metall. Sin. (Engl. Lett.) **23**, 301 (2010)
[19] J.L. Youngblood, M. Raghava, Metall. Trans. A **8**, 1439 (1977)
[20] R. Padmanhan, W.E. Wood, Mater. Sci. Eng. A **66**, 125 (1984)
[21] B.G. Pound, Acta Mater. **46**, 5733 (1998)
[22] D. Figueroa, M.J. Robinson, Corros. Sci. **52**, 1593 (2010)
[23] The American Standard for Testing and materials, ASTM G44-99 (1999)
[24] M. Hanesch, Geophys. J. Int. **177**, 941 (2009)
[25] D.L.A. de Faria, S. Venancio Silva, M.T. de Oliveira, J. Raman Spectrosc. **28**, 873 (1997)
[26] R.J. Thibeau, C.W. Brown, R.H. Heidersbach, Appl. Spectrosc. **32**, 532 (1978)
[27] J.R. Ferraro, K. Nakamoto, C.W. Brown, *Introductory Raman Spectroscopy: Basic Theory* (Academic Press, Beijing, 2003)
[28] E. Hazan, Y. Sadia, Y. Gelbstein, Corros. Sci. **74**, 414 (2013)
[29] K. Asami, M. Kikuchi, Corros. Sci. **45**, 2671 (2003)
[30] H. Tamura, Corros. Sci. **50**, 1872 (2008)